

# Two 3D Cd(II) Metal–Organic Frameworks Linked by Benzothiadiazole Dicarboxylates: Fantastic S@Cd<sub>6</sub> Cage, Benzothiadiazole Antidimmer, and Dual Emission

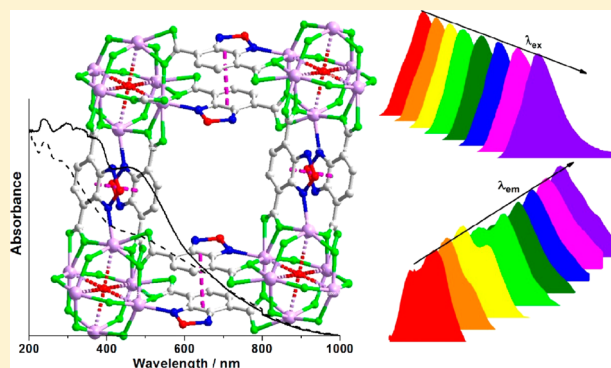
Qing Cheng,<sup>†,‡</sup> Xiao Han,<sup>†,‡</sup> Yue Tong,<sup>†</sup> Chao Huang,<sup>‡</sup> Jie Ding,<sup>\*,†</sup> and Hongwei Hou<sup>\*,†</sup>

<sup>†</sup>College of Chemistry and Molecular Engineering, Zhengzhou University, Henan 450001, P. R. China

<sup>‡</sup>Center for Advanced Materials Research, Zhongyuan University of Technology, Zhengzhou 450007, P. R. China

## Supporting Information

**ABSTRACT:** On the basis of the same benzothiadiazole (BTD) ligand 2,1,3-benzothiadiazole-4,7-dicarboxylic acid (H<sub>2</sub>L), two new isomers of three-dimensional (3D) BTD-derived Cd(II) metal–organic frameworks 1–2 {[S@Cd<sub>6</sub>L<sub>6</sub>]·xH<sub>2</sub>O}<sub>n</sub> were obtained by the different solvothermal reactions, which were structurally similar. Surprisingly, structural analyses reveal that in 1 or 2, one free sulfur atom was fixed in a Cd(II) cluster cage by strong intermolecular interaction to form the secondary building unit (SBU) S@Cd<sub>6</sub>. Each SBU S@Cd<sub>6</sub> is connected by six L<sup>2-</sup> ligands and further extended into the 3D porous framework. In this work, the BTD antidimmer was evidenced by structural analysis and photophysical study. Furthermore, either 1 or 2 showed the uncommon dual emission, while only one emission was observed in the solution of ligand H<sub>2</sub>L. The dual-emission mechanism was also realized by the structural analysis and photophysical study. Interestingly, although there is slight difference in structure (regular octahedral cage in 1 and slightly distorted octahedral cage in 2), the changes in N<sub>2</sub> adsorption capability and photophysical performance between 1 and 2 are obvious, where 2 shows smaller Brunauer–Emmett–Teller surface area, broader absorption of antidimmer, and longer dual-emission lifetimes. Interestingly, either 1 or 2, the dual emission was clearly red-shifted by increasing the solvent polarity or the acidity of ambience, respectively.



## INTRODUCTION

Undoubtedly, metal–organic framework (MOF), an attractively versatile platform for achieving long-range organization and order as well as exploitable property,<sup>1,2</sup> has been attracting the gazes of many chemists and material scientists during the past decade.<sup>3–5</sup> In particular, such optical-functional systems were gradually used to explore the amazing applications,<sup>6,7</sup> such as light-emitting devices,<sup>8</sup> light-harvester,<sup>9</sup> nonlinear optics,<sup>10</sup> photocatalysis,<sup>11,12</sup> and sensor technology.<sup>13,14</sup> Since then, we are very interested in constructing new chromophore-derived MOF and exploring the relationship between photophysical properties and the structures to get the excellent optical-functional materials. In our previous work of BODIPY-derived MOF, the special coordination modes are capable of forming the two BODIPY units in coplanar arrangements to display the uncommon J-dimer absorption band.<sup>15</sup>

Herein, 2,1,3-benzothiadiazole (BTD), another famous  $\pi$ -conjugated chromophore,<sup>16–19</sup> was selected to construct a new series of optical-functional MOFs. Actually, BTD derivative is normally efficient chromophore with high fluorescence quantum yield. Meanwhile, because of the strong electron-withdrawing capacity of heterocyclic unit as well as relatively high reduction potential, such derivative is a possible electron

carrier or electron acceptor. Especially, the highly polarized feature of BTD species usually supports it to afford well-ordered crystal structure by intermolecular interactions (such as heteroatom contacts and  $\pi$ – $\pi$  interactions).<sup>16f</sup> When planar BTD units are held in a cofacial geometry at a suitable distance in crystalline state, it is appropriate to observe the photophysical behavior of uncommon dimer.<sup>20</sup> Until now, despite the intriguing properties, only Chen group reported few BTD-derived Nd-MOFs for enhanced CO<sub>2</sub> sorption.<sup>21</sup> In this relatively unexplored area, elaborate design and deep photophysical research will be beneficial for the fast development of optical-functional BTD-derived MOF material.

In this paper, we selected the analogue of famous “terephthalic acid”, 2,1,3-benzothiadiazole-4,7-dicarboxylic acid (H<sub>2</sub>L), as the linker to construct new BTD-derived MOF. Herein, two novel MOF 1 and 2 were successfully obtained with the same BTD ligand. It is surprising that in the structurally similar MOFs 1 and 2, one free sulfur atom was fixed in a Cd(II) cluster cage to form the secondary building unit (SBU) S@Cd<sub>6</sub>. Each SBU S@Cd<sub>6</sub> is connected by six L<sup>2-</sup>

Received: November 25, 2016

ligands and further extended into a three-dimensional (3D) porous framework. In this work, the two adjacent BTD units are held in an antidimmer mode with the transannular distance from 3.47 to 3.49 Å (shorter than the value of theoretical prediction) that was further evidenced by the corresponding photophysical study. Furthermore, either **1** or **2** showed the uncommon dual emission, while only one emission was observed in the solution of ligand **H<sub>2</sub>L**. The dual-emission mechanism was also realized by the structural analysis and photophysical study. More interestingly, although there is slight difference in structure, the photophysical performance change between **1** and **2** is distinct, where broader antidimmer absorption is observed in **2** as well as longer dual-emission lifetimes.

## EXPERIMENTAL SECTION

**Materials.** All chemical reagents were purchased from commercial suppliers without further purification. For 2,1,3-benzothiadiazole-4,7-dicarboxylic acid (**H<sub>2</sub>L**), the synthetic procedure is according to the literature (Scheme S1).<sup>22</sup>

**Physical Measurements.** <sup>1</sup>H NMR (400 MHz) spectra were measured on a Bruker Avance-400 nuclear magnetic resonance (NMR) spectrometer. Thermal stability studies were performed on a Netzsch STA 449C thermal analyzer at a heating rate of 10 °C/min, from 30 to 900 °C under the air atmosphere. Power X-ray diffraction (PXRD) patterns were measured on a PANalytical X'Pert PRO diffractometer with Cu Kα1 radiation. The results from the PXRD patterns are in close agreement with those calculated from the single-crystal structure determination. The gas sorption isotherms of coordination polymers **1** and **2** were collected on a Micromeritics 3Flex surface area and pore size analyzer under ultrahigh vacuum in a clean system, with a diaphragm and turbo pumping system. Ultrahigh-purity (>99.999%) N<sub>2</sub> gas was applied in all adsorption measurements. The experimental temperature was maintained by liquid nitrogen (77 K). Prior to measurement, supercritical CO<sub>2</sub> (SC-CO<sub>2</sub>) activation was used to remove the solvent molecules in samples **1** and **2** by a custom-built system. Typically, bulk sample of complex **1** was washed by absolute ethanol (EtOH) three times, dried under vacuum, and then transferred into stainless steel column. After 20 min of soaking and venting of supercritical CO<sub>2</sub> by a DB-80 simplex pump, the column pressure regulator was set at 100 bar by soaking SC-CO<sub>2</sub>, and the column temperature was raised to 40 °C. SC-CO<sub>2</sub> in the column was gradually vented after 14 h. The activation samples were placed in sealed containers for nitrogen adsorption. Thermogravimetric analysis (TGA) experiments and PXRD were performed to make sure that the solvent molecules were removed completely and the framework structures retained crystallinity after activation, respectively.

Single-crystal X-ray data for compounds **1** and **2** were collected on a Rigaku Saturn 724 CCD diffractometer equipped with a graphite monochromator and Mo Kα (λ = 0.710 73 Å, 293 ± 1 K) radiation. Data collections were performed using φ and ω scan. Non-hydrogen atoms located from the difference Fourier maps were refined anisotropically by full-matrix least-squares on F<sup>2</sup>, using SHELXS-97.<sup>23</sup> All hydrogen atoms were included in the calculated positions and refined isotropically using a riding model. Determinations of the crystal system, orientation matrix, and cell dimensions were performed according to the established procedures. Lorentz polarization and multiscan absorption correction were applied. All calculations were performed using SHELXL 97 and PLATON 99. The numbers of guest molecules for **1** and **2** were calculated by the TGA. The crystallographic data for **1** and **2** are listed in Table 1. Moreover, the selected bonds distances and bond angles are summarized in Supporting Information Table S1.

**Photophysical Measurements.** The UV–vis absorption spectra in the solid state were measured by a Cary 5000 spectro-photometer equipped with a 110 nm diameter integrating sphere. Spectra in the solution were measured by an equipped V-750 spectro-photometer. The measurements of steady-state emission spectra in the solid state

**Table 1. Crystallographic Data and Structure Refinement Details for Complexes 1 and 2**

complex	1	2
formula	C <sub>48</sub> H <sub>30</sub> N <sub>12</sub> O <sub>33</sub> S <sub>7</sub> Cd <sub>6</sub>	C <sub>48</sub> H <sub>24</sub> N <sub>12</sub> O <sub>30</sub> S <sub>7</sub> Cd <sub>6</sub>
fw	2201.66	2147.61
T/K	293	293
crystal system	trigonal	trigonal
space group	R $\bar{3}$	R $\bar{3}$
a (Å)	19.676(3)	19.377(3)
b (Å)	19.676(3)	19.377(3)
c (Å)	19.300(4)	19.810(4)
α (deg)	90	90
β (deg)	90	90
γ (deg)	120	120
V (Å <sup>3</sup> )	6471(2)	6442(2)
Z	3	3
D <sub>calcd</sub> (g·cm <sup>-3</sup> )	1.695	1.661
abs coeff (mm <sup>-1</sup> )	1.701	1.704
F (000)	3198.0	3108.0
GOF	1.080	1.116
data/restraints/parameters	3401/0/165	3413/0/165
R <sub>1</sub> (I > 2σ(I)) <sup>a</sup>	0.0366	0.0401
wR <sub>2</sub> (I > 2σ(I)) <sup>b</sup>	0.0906	0.1017

<sup>a</sup>R<sub>1</sub> =  $\sum ||F_o| - |F_c|| / \sum |F_o|$ . <sup>b</sup>wR<sub>2</sub> =  $\{\sum [w(F_o^2 - F_c^2)^2] / \sum [w(F_o^2)]\}^{1/2}$ .

were conducted on a FL-4600 fluorescence spectro-photometer at room temperature. The emission decay lifetime was measured on an Edinburgh instrument FLS980 fluorescence spectrometer. In this emission lifetime experiment, two excitation wavelengths were chosen. Under the irradiation of 330 nm light, the tested emission lifetime wavelength range is from 350 to 450 nm with 20–30 nm intervals (those are 350, 370, 390, 410, 430, 450, 480, 500, 520, 540, 560, 580, 600, and 620 nm), while another emission lifetime wavelength range is 500–620 nm with 20 nm interval (those are 500, 520, 540, 560, 580, 600, and 620 nm) excited at 405 nm. Herein, the details of fitting results were in the Supporting Information (Table S2).

**Synthesis of [S@Cd<sub>6</sub>L<sub>6</sub>]-9H<sub>2</sub>O]<sub>n</sub> (**1**).** **H<sub>2</sub>L** (0.1148 g; 0.5 mmol) and CdCl<sub>2</sub> (0.2284 g, 1 mmol) were dissolved separately in dimethylformamide (DMF)/H<sub>2</sub>O (10:10, v/v) solution. Meanwhile, 10 mL of adenine (0.0405 mol L<sup>-1</sup>) DMF solution was also prepared, and mixed with the **H<sub>2</sub>L** and CdCl<sub>2</sub>, DMF/H<sub>2</sub>O (10:10, v/v) solutions. Each 0.5 mL of the above mixed solution was added to 3.5 mL of DMF/EtOH (1.5/2, v/v) solution in a 10 mL glass tube. The reaction mixture was heated at 80 °C for 3 d. After the cooling treatment, red-brown crystals of **1** were washed several times with mother liquor and dried (yield: 72%, based on **H<sub>2</sub>L** ligand). Anal. Calcd for C<sub>48</sub>H<sub>30</sub>Cd<sub>6</sub>N<sub>12</sub>O<sub>33</sub>S<sub>7</sub> (%): C, 26.16; H, 1.36; N, 7.63. Found (%): C, 26.31; H, 1.07; N, 7.77. IR data (KBr, ν/cm<sup>-1</sup>): 3440 (s), 1584 (s), 1497 (w), 1401 (s), 1313 (m), 1222 (w), 1112 (w), 1040 (w), 905 (w), 838 (m), 828 (m), 818 (m), 779 (m), 665 (w), 623(w), 573 (w), 479 (w).

**Synthesis of [S@Cd<sub>6</sub>L<sub>6</sub>]-6H<sub>2</sub>O]<sub>n</sub> (**2**).** A mixture containing Cd(NO<sub>3</sub>)<sub>2</sub>·4H<sub>2</sub>O (0.0308 g, 0.1 mmol) and **H<sub>2</sub>L** (0.0224 g, 0.1 mmol) was dissolved in 5 mL of DMF/EtOH/H<sub>2</sub>O (1:2:2, v/v/v). The mixture was heated at 120 °C in a 20 mL Teflon-lined autoclave for 3 d. After the cooling treatment, reddish-brown crystals of **2** were separated and washed with mother liquor (yield: 80%, based on **H<sub>2</sub>L** ligand). Anal. Calcd for C<sub>48</sub>H<sub>24</sub>Cd<sub>6</sub>N<sub>12</sub>O<sub>30</sub>S<sub>7</sub> (%): C, 26.82; H, 1.12; N, 7.82. Found (%): C, 26.50; H, 1.55; N, 7.71. IR data (KBr, ν/cm<sup>-1</sup>): 3316 (s), 1579 (s), 1542 (s), 1401 (s), 1386 (s), 1312 (s), 1221 (w), 1145 (w), 1031 (w), 871 (w), 834 (m), 779 (m), 624 (w), 570 (w), 476 (w).

## RESULTS AND DISCUSSION

As we know, the ligand terephthalic acid is a super linker. In this platform, many MOFs were constructed, including the

famous pioneer MOF-5. However, because of the structural character of terephthalic acid, the direct application in optical-functional material was limited. In this work, we selected one analogue of terephthalic acid, 2,1,3-benzothiadiazole-4,7-dicarboxylic acid ( $H_2L$ ), as the linker to construct optical-functional BTD-derived MOF. Herein, two new BTD-derived MOFs **1** and **2** were successfully obtained with the same chromophore linker  $H_2L$  by the different solvothermal reactions, respectively. In the DMF/EtOH/ $H_2O$  (2.5:2:0.5, v/v/v) media, complex **1** crystallizes in a hexagonal system with non-centrosymmetric  $R\bar{3}$  space group. As shown in Figure S1, there are four separated Cd(II) ions, one deprotonation  $L^{2-}$  ligand in the asymmetric unit of **1**, where each of Cd(II) ions adapts an octahedral geometry. In this Cd-MOF, it is notable that adenine is not an auxiliary ligand but possibly a template agent. In addition, both of the carboxylic groups in the ligand adopt  $\mu_2$ - $\eta^2$ -chelate/bridge coordination fashions. Surprisingly, one free sulfur atom S2 was fixed in an octahedral Cd(II) cluster cage, which was formed by six Cd(II) ions. In this regularly octahedral cage, the distance of Cd–S2 was 2.88 Å, which was longer than a typical Cd–S bond.<sup>24</sup> As we know, the precursor ( $BBr_2$ ) of ligand  $H_2L$  was derived by *o*-phenylenediamine.<sup>25</sup> Hence, in the solvothermal condition, it was possible that a few free sulfur atoms were produced by the dissociation of the ligand, which further were trapped in Cd(II) cluster cage. Furthermore,  $S@Cd_6$  cage is also the secondary building unit (SBU; Figure 1). Each SBU  $S@Cd_6$  is connected by six  $L^{2-}$

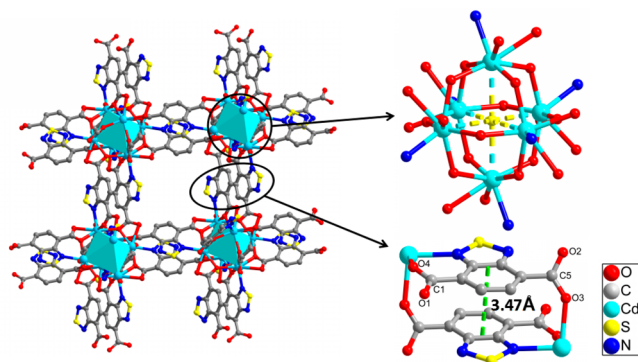


**Figure 1.** Schematic representation of the structure of complex **1**. Hydrogen atoms and solvent molecules were omitted for clarity.

ligands and further extended into the 3D porous framework (Figure 1; the perspective view and topology of **1** was shown in Figure S1). This pore is regular, the size of which is  $13.1 \times 13.1 \times 13.1 \text{ \AA}^3$ .

The dihedral angle is  $46.8^\circ$  between the plane of O4, C1, and O1 and plane of O2, C5, and O3 (Figure 1). Significantly, the two adjacent chromophore linkers (BTD unit) are held in a cofacial geometry (in opposite direction, antimode) with the transannular distance of 3.47 Å. This transannular distance is shorter than the distance of antidimer predicted by theoretical calculation (4.00 Å),<sup>20a</sup> but it is longer than that in anti-[2.2](4,7)benzothiadiazolophane (average distance 2.94 Å).<sup>20b</sup> Herein, we preliminarily inferred that there was BTD antidimer in the complex **1**. As shown in Figure S2, the peak positions of the experimental PXRD spectrum match well with that of simulated one, indicating the excellent phase purity of complex **1**. In addition, application of the SQUEEZE routine in PLATON indicates a void volume of 29% in the total cell volume. These channels are probably occupied by solvents, which are further confirmed by TGA. From the TGA experiment (Figure S3), there are two successive weight losses of 8.83% (calcd 8.81%) before  $190^\circ\text{C}$ . It is ascribed to the absence of solvents in the cavity and free S atom in the  $S@Cd_6$  cage, which was further supported by the result from  $^1\text{H}$  NMR spectrum for complex **1** immersed in  $\text{CD}_3\text{CN}$  for one week (the DMF signal was resulted from the DMF molecules adhered in the surface of crystal, Figure S4). Over  $190^\circ\text{C}$ , the framework of sample **1** was decomposed gradually, which was also proved by the PXRD patterns for complex **1** heated under  $130^\circ\text{C}$  and  $180^\circ\text{C}$ , respectively (Figure S2). Thus, gas sorption measurement for the as-synthesized sample **1** after  $\text{SC}-\text{CO}_2$  activation was conducted up to a relative pressure ( $p/p_0$ ) of 1.0 on the activated frameworks at STP.  $\text{N}_2$  adsorption isotherm demonstrates that MOF **1** exhibited the Brunauer–Emmett–Teller (BET) surface area of  $404.34 \text{ m}^2/\text{g}$  (Figure S5). Interestingly, MOF **1** showed the good chemical stability (Figure S2) in intermediate acidic ( $\text{pH} = 3$ ) or basic condition ( $\text{pH} = 11$ ).

It is interesting that without adenine in similar DMF/EtOH/ $H_2O$  (1:2:2, v/v/v) media, when the solvothermal reaction temperature raised to  $120^\circ\text{C}$  and  $\text{CdCl}_2$  was replaced by  $\text{Cd}(\text{NO}_3)_2 \cdot 4\text{H}_2\text{O}$ , Cd-MOF **2** crystallized in the same hexagonal crystal system with non-centrosymmetric  $R\bar{3}$  space

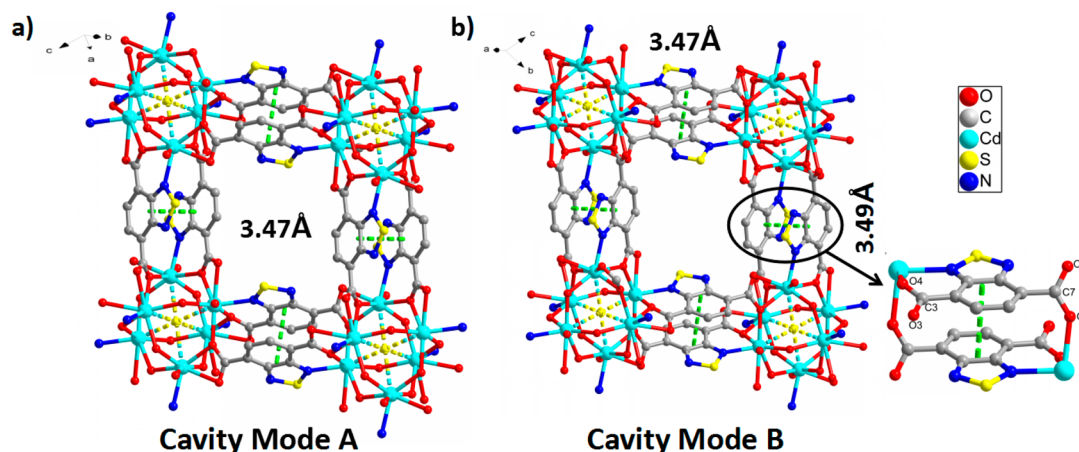


**Figure 2.** Schematic representation of the structures of **2**, where hydrogen atoms and solvent molecules were omitted for clarity. (a) Cavity mode A. (b) Cavity mode B.

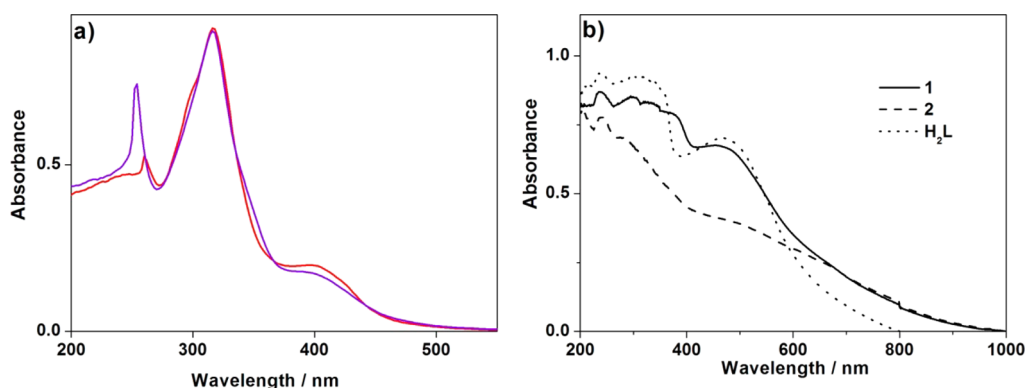


**Figure 3.** (a) UV-vis absorption spectra of  $\text{H}_2\text{L}$  in the DMF/EtOH/ $\text{H}_2\text{O}$  (2.5:2:0.5, v/v/v, red) media and DMF/EtOH/ $\text{H}_2\text{O}$  (1:2:2, v/v/v, violet) media at room temperature, and (b) UV-vis absorption spectra of **1** (solid line), **2** (dash line), and  $\text{H}_2\text{L}$  (dot line) in solid state at room temperature.

group. More surprisingly, there are many similarities in the structures of **1** and **2**. For instance, the asymmetric unit of **2** also contains four separated Cd(II) ions, one deprotonation  $\text{L}^{2-}$  ligand (Figure S1). As shown in Figure S6, one S2 atom was also surrounded by six Cd(II) ions to form a cage core  $\text{S}@\text{Cd}_6$ , which topologically serves as an uncommon 6-connecting node to further form a porous 3D framework. Moreover, the parallelogram-shaped cage of **2** is of  $13.0 \times 13.0 \times 13.0 \text{ \AA}^3$ . Notably, although the  $\text{L}^{2-}$  ligands in **1** and **2** adopt the same coordination mode (Figures S1 and S6), the Cd(II) ion in **2** possesses a slightly distorted octahedral fashion. Normally, the  $\text{S}@\text{Cd}_6$  SBU in **2** is a distorted octahedral geometry, in which the distance of Cd–S2 is in the range of 2.878–2.880 Å. As a consequence, there were two cavity modes (cavity mode A and cavity mode B, Figure 2). In cavity mode A, the transannular distance of two adjacent BTD units is completely equal (3.47 Å, Figure 2a) with complex **1**. In contrast, in cavity mode B, the dihedral angle between the plane of O4, C3, and O3 and plane of O1, C7, and O2 is 45.6°, which results in the transannular distance of two adjacent BTD units being incompletely equal (3.47 and 3.49 Å; Figure 2b). Hence, it is foreseeable that different from that in complex **1**, there were probably two kinds of BTD antidimmer in the complex **2**. In addition, the phase purity was confirmed by the PXRD analyses (Figure S7). Because of the similarities in the structure, the framework of sample **2** was decomposed gradually in similar temperature, which was proved by the TGA and variable-temperature PXRD results (Figures S3 and S7). There is a void volume of 29% in the total cell demonstrated by the SQUEEZE routine in PLATON. Additionally, in  $^1\text{H}$  NMR spectrum for complex **2** immersed in  $\text{CD}_3\text{CN}$  for one week (Figure S4), the water signal with lower intensity compared to that in **1** also indicated the presence of crystalline water molecules, while weak DMF signal resulted from the DMF molecules adhered in the surface of crystal. Surprisingly, because of the slight difference in structure, the BET surface area of  $102.23 \text{ m}^2/\text{g}$  (Figure S8) was distinctly smaller than that of **1**, which was calculated from  $\text{N}_2$  adsorption isotherm of **2**. Moreover, MOF **2** also showed the good chemical stability in intermediate acidic or basic condition (Figure S7).

**Photophysical Behavior Study.** As described above, in complex **1** or **2**, the two adjacent chromophore linkers (BTD unit) are held in a cofacial geometry (antimode), where the transannular distance is shorter than the value of theoretically predicted antidimmer.<sup>20a</sup> This structural character may induce

some interesting photophysical properties that are different than those of monomeric  $\text{H}_2\text{L}$  in solution. In this work, the solution UV-vis absorption spectra (Figure 3a) of  $\text{H}_2\text{L}$  and the solid-state UV-vis absorption spectra (Figure 3b) of **1**, **2**, and  $\text{H}_2\text{L}$  were measured at room temperature.

As shown in Figure 3a, the ligand  $\text{H}_2\text{L}$  actually showed very similar behaviors in DMF/EtOH/ $\text{H}_2\text{O}$  (2.5:2:0.5, v/v/v, reaction solvent for the preparation of complex **1**) and DMF/EtOH/ $\text{H}_2\text{O}$  (1:2:2, v/v/v, reaction solvent for the preparation of complex **2**), because of similar absorption spectrum of ligand  $\text{H}_2\text{L}$  in pure DMF, EtOH, or  $\text{H}_2\text{O}$  media (Figure S9a). There are several intense absorption bands before 370 nm and one intermediate absorption band around 400 nm. In addition, the intensity of absorption band around 400 nm can be fitted by the Lambert–Beer Law (in the absorbance range of 0–1, Figure S9b), indicating that this lowest-energy excited state is ascribed to the monomeric  $\text{H}_2\text{L}$  species polarized by highly polar solvent. In contrast, in power sample  $\text{H}_2\text{L}$ , one new absorption band in the lower energy level was observed at 470 nm, while such three bands observed in solution were visibly blue-shifted. The blue-shifted  $\pi \rightarrow \pi^*$  transition of monomeric BTD group could be resulted from the absence of the solvent polarization interaction. Because power sample  $\text{H}_2\text{L}$  was amorphous, there was no clear structure information to reveal the feature of the new absorption band at 470 nm. Thus, although it is tempting to ascribe such band to  $\pi\text{--}\pi$  stacking, we need to do more experiments with caution before drawing any conclusions.

More interestingly, similar behaviors also were displayed in both crystalline samples **1** and **2**. For complexes **1** and **2**, the mechanism of shifted monomeric BTD absorption band was complicated, which might mainly be influenced by the changed electron-withdrawing character of carboxylate groups at the 4,7-positions by being coordinated with transition metal ion<sup>15</sup> as well as the polarization interaction of remaining solvent in the cavity. In addition, in comparison with powder sample  $\text{H}_2\text{L}$ , there was a prolonged tail of absorption around 470 nm in either **1** or **2**. Especially in case **2**, such absorption band was broadened to lose some feature of peak. As we know, the BTD unit is commonly planar that distinctly enhances the odds of  $\pi\text{--}\pi$  stacking in solid state. As exhibited in Figures 1 and 2, only the coplanar BTD moieties were observed in complex **1** or **2**. The transannular distance was approximately in the range of strong  $\pi\text{--}\pi$  interaction, which was also shorter than the value of theoretically predicted antidimmer. Hence, such absorption

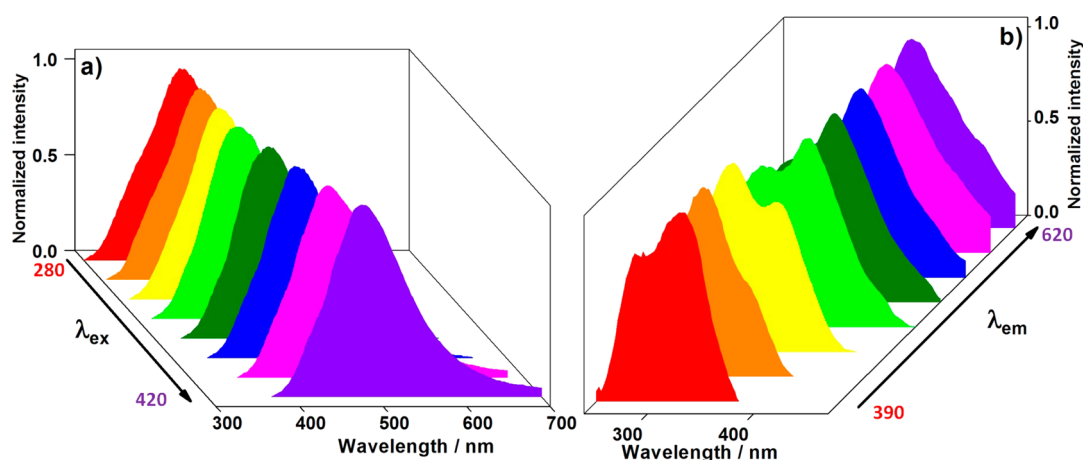


**Figure 4.** (a) Emission and (b) excitation spectra of **1** in the solid state at room temperature ( $\lambda_{\text{ex}} = 280$  nm, red; 300 nm, orange; 320 nm, yellow; 340 nm, green; 360 nm, olive; 380 nm, blue; 400 nm, magenta; 420 nm, violet.  $\lambda_{\text{em}} = 390$  nm, red; 420 nm, orange; 460 nm, yellow; 500 nm, green; 520 nm, olive; 540 nm, blue; 580 nm, magenta; 620 nm, violet).

band around 470 nm (Figure 3b) is clearly assigned by the transition of antidimmer. In comparison with **1**, because of two kinds of BTD antidimmer in the complex **2**, the broad absorption band of antidimmer is actually including more than one peak.

Commonly, more sensitive emission spectroscopic experiment comparing to absorption test could demonstrate the further detail for photophysical performance of sample (Figure 4, Table 2, Figures S13). In this work,  $\text{H}_2\text{L}$  dilute solution

**Table 2. Absorption and Steady-State Fluorescence Properties of Crystals **1**, **2**, Power  $\text{H}_2\text{L}$ , and  $\text{H}_2\text{L}$  Solution at Room Temperature**

sample	$\lambda_{\text{ab}}$ , nm	$\lambda_{\text{em}}$ , nm	$\tau_{\text{F}}$ , ns
<b>1</b>	236, 292–333 <sup>b</sup> , 372, 468	418, >520 <sup>a</sup>	2.3, 5.5
<b>2</b>	205, 284–328 <sup>b</sup> , 372, 480	418, >540 <sup>a</sup>	2.5, 7.8
$\text{H}_2\text{L}^{\text{d}}$	209, 236, 312–356 <sup>b</sup> , 470	<i>c</i>	<i>c</i>
$\text{H}_2\text{L}^{\text{e}}$	260, 284–348 <sup>b</sup> , 396	467, 486	<i>c</i>
$\text{H}_2\text{L}^{\text{f}}$	254, 284–348 <sup>b</sup> , 394	474, 489	<i>c</i>

<sup>a</sup>Because of the bad signal resolution under in the irradiation of light (>420 nm), the position of this emission peak was not clear. <sup>b</sup>Broad signal including multipeaks. <sup>c</sup>Not measured in this paper. <sup>d</sup>The powder sample. <sup>e</sup>In the DMF/EtOH/ $\text{H}_2\text{O}$  (2.5:2:0.5, v/v/v) media. <sup>f</sup>In the DMF/EtOH/ $\text{H}_2\text{O}$  (1:2:2, v/v/v) media.

showed the emission with one shoulder peak excited in the range of 260–440 nm, where the valley of intensity was observed in the irradiation of 320 nm. The peaks of emission intensity were observed in the irradiation of 280 and 396 nm, respectively. The corresponding excitation spectra also indicated that the light in the range of 310–330 nm was almost no contribution for the sample emission. Furthermore, the light at 282 nm ( $\nu = 35\,450\text{ cm}^{-1}$ ) or 390 nm ( $\nu = 25\,650\text{ cm}^{-1}$ ) was the most powerful supporter for the emission. These results proved that (a) there was only one emission in the  $\text{H}_2\text{L}$  dilute solution, which was ascribed to the lowest-energy  $\pi \rightarrow \pi^*$  transition of monomeric BTD group ( $\nu = 25\,650\text{ cm}^{-1}$ ); and (b) because of the relatively big energy gap ( $\sim 9800\text{ cm}^{-1}$ , 1.22 eV), the main decay of transition around  $35\,400\text{ cm}^{-1}$  was not irradiation decay but internal conversion (IC) that transferred the energy to the lowest-energy transition of monomeric BTD group.

Surprisingly, when the ligand  $\text{H}_2\text{L}$  was coordinated with Cd(II) ion, either complex **1** or **2** showed the totally different emission behavior (Figure 4 and Figure S13) in comparison with that of  $\text{H}_2\text{L}$  in solution. Unfortunately, excited at 470 nm, neither **1** nor **2** was absent of antidimmer emission. As we knew, large Stokes shift is common in BTD-based species; therefore, such emission was probably in near-infrared (NIR) range. Moreover, it totally quenched in concentrated solid state. As shown in Figure 4a, when the excitation light shifted to longer wavelength, the emission peak was also red-shifted. This phenomenon is uncommon, indicating that more than one emissive excited state is present in the system. At the same time, in the corresponding excitation spectroscopic experiments, the emission at 500 nm is like a “watershed”. The emission before 500 nm was mainly contributed by the transition centered at 316 nm ( $\nu = 31\,650\text{ cm}^{-1}$ ), while the emission after 500 nm was mainly contributed by the transition centered at 372 nm ( $\nu = 26\,900\text{ cm}^{-1}$ ). In comparison with  $\text{H}_2\text{L}$  dilute solution, the energy gap shortens ( $\sim 4750\text{ cm}^{-1}$ , 0.59 eV) shown in the excitation spectra of complex **1**, and the overlap is also visible. Hence, from these results, it is reasonable that the decay way of transition centered at 316 nm was not only IC but also irradiation decay. This conclusion needs to be further confirmed by the emission lifetime study (Table 2 and Table S2).

Emission decay curves were measured in solid state at room temperature with irradiation at 330 nm ( $30\,300\text{ cm}^{-1}$ ) or 405 nm ( $24\,700\text{ cm}^{-1}$ ) detection at different wavelengths across the emission spectrum. Excited at 330 nm, the logarithmic plot shows a typical single-exponential behavior (for **1**: 2.3 ns; for **2**: 2.5 ns). In contrast, when complex **1** under the irradiation of 405 nm light, double exponential fitting was the best choice, with a fast component ( $\tau_1 \approx 1.9\text{ ns}$ ) and a slower component ( $\tau_2 = 5.5\text{ ns}$ ). The full analysis of the decay curves (see Table S2 in the Supporting Information) confirms that more than 60% of the observed luminescence is due to the slow component at lower energy level. Similarly, with complex **2** excited at 405 nm, double exponential fitting was also appropriate with a fast component ( $\tau_1 \approx 2.1\text{ ns}$ ) and a slower component ( $\tau_2 = 7.8\text{ ns}$ ). In this case, more than 74% of the observed luminescence is due to the slow component at lower energy level.

At last, from the structural and spectroscopic information, we can sketch a model for the understanding this dual-emission

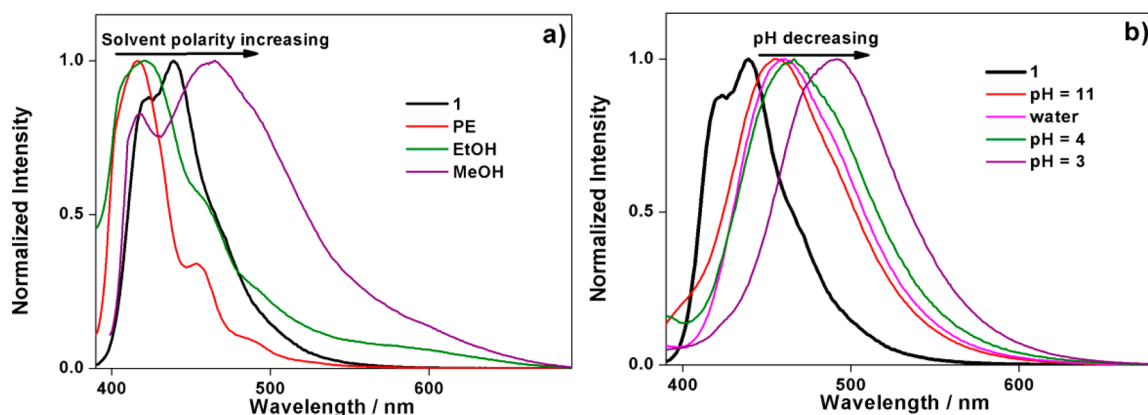


**Figure 5.** (a) Emission spectra of **1** in solid state (black bolded) and ground **1** dispersed in different organic solvents (red: in petroleum ether; olive: in ethanol; and violet: in methanol); (b) emission spectra of **1** in solid state (black bolded) and ground **1** dispersed in different aqueous media at room temperature (red: in ambience of pH = 11, sodium hydroxide aqueous solution; magenta: in water; olive: in ambience of pH = 4, nitric acid aqueous solution; and violet: in ambience of pH = 3, nitric acid aqueous solution).  $\lambda_{\text{ex}} = 370$  nm.

mechanism. Different from the ordinary emission mechanism model in  $\text{H}_2\text{L}$  dilute solution (Figure S14a), complex **1** or **2** after the excitation process showed that the decay of excited state at higher-energy level (centered at 316 nm,  $\nu = 31\,650\text{ cm}^{-1}$ ) could be accomplished by IC to lower-energy excited state of monomeric BTD group or lowest-energy excited state of BTD antidimmer, while the irradiation decay process (fluorescence) was also allowed. For the decay of excited state at lower-energy level (centered at 372 nm,  $\nu = 26\,900\text{ cm}^{-1}$ ) in complex **1** or **2**, there were still two main processes, namely, IC to lowest-energy excited state of BTD antidimmer and irradiation decay. In contrast, the lowest-energy excited state of BTD antidimmer was decayed by a non-irradiation way. In comparison with **1**, the longer dual-emission lifetimes observed in **2** probably resulted from the enhanced IC process to suppress non-irradiation decay, since there were two kinds of BTD antidimmer in the complex **2**. More importantly, even after the  $\text{SC-CO}_2$  activation procedure, both **1**-desolvated and **2**-desolvated still displayed the similar dual-emission feature as well as the similar absorption bands (Figures S15 and S16), in comparison with either **1** or **2**. It is possibly ascribed to only crystalline water in the cavity of sample MOF before solvent-removal procedure.

As we know, chromophore molecule commonly shows the interesting solvatochromic behavior in solution, which is originated from the feature easily polarized by the ambient solvent molecules. As follows, the corresponding emission also is influenced by the ambient solvent molecules. Herein, because comparing to the relatively free solution environment, the arrangement of chromophore species was restricted by the center metal ion in porous MOF; the solvatochromic behavior research may reveal more information from the connection between photophysical property and the structure. In this work, a series of organic solvents (petroleum ether, toluene, ethanol, ethyl acetate, dioxane, acetone, methanol, and ethylene glycol) and different aqueous media (pH = 3, pH = 4, pure water, and pH = 11) were chosen for the solvatochromic behavior research (Figure 5 and Figures S17–S22). In comparison with the similar solvatochromic behavior of **2**, that of MOF **1** was more pronounced; thus, the detail was described below. Although there was a slight shift in the lowest-energy absorption band, the change of emission behavior in MOF **1** was distinctly visible. As shown in Figure 5a, under the irradiation of 370 nm

light, pure MOF **1** showed a dual-emission performance ( $\lambda_{\text{em}} = 423, 439$  nm), while this dual emission was clearly red-shifted by increasing the solvent polarity. More interestingly, the large red-shift of emissive excited state with lower energy ( $\lambda_{\text{em}} = 439$  nm) was observed compared to that of emissive excited state with higher energy ( $\lambda_{\text{em}} = 423$  nm). Such change should be attributed to the emissive excited states with higher energy ( $\lambda_{\text{em}} = 439$  nm) that displayed some charge transfer (CT) character after the coordination between ligand  $\text{H}_2\text{L}$  and center metal Cd(II) ion. Moreover, this red-shift phenomenon was much more pronounced in aqueous media, from blue region to green region, which was observed by increasing the acidity of ambience (Figure 5b). In addition, after 8 h immersed in acidic or basic media, this phenomenon still was the same as the initial state of MOF **1** (Figure S21), which was consistent with the result from the PXRD experiment (Figure S2). Before considering any hypothesis of the solvatochromic mechanism in aqueous media, the control experiment of ligand  $\text{H}_2\text{L}$  was accomplished in same condition. As shown in Figure S23a, there was a slight shift in the lowest-energy absorption band in different aqueous solution of ligand  $\text{H}_2\text{L}$ . The red-shifted emission in ligand  $\text{H}_2\text{L}$  was distinctly observed by increasing the acidity of ambience (Figure S23b), whereas the change of excitation spectra was slightly (Figure S23c) that was consistent to the absorption spectra. As we know, the BTD species is a typical electron acceptor. When pH-sensitive carboxyl group and N atoms in BTD species were under the acidic condition, the electron-donating capability of carboxyl group and the electron-withdrawing capability of BTD species were amplified, respectively. It resulted in an enhancing CT character of lowest-energy excited state in ligand  $\text{H}_2\text{L}$  under the acidic condition with small energy gap comparing to that in pure water system. In contrast, under the basic condition, the deprotonated carboxyl group was a weak electron acceptor, while the electron-withdrawing capability was weakened in BTD species. This result indicated a large energy gap of lowest-energy excited state in ligand  $\text{H}_2\text{L}$  under the basic condition with negligible CT character compared to that in pure water system. Similarly, we surmised that the electron distortion of noncoordinated N atoms in **1** under the acidic or basic condition was probably an important factor, which might trigger the whole electron arrangement change of the coordinated ligand  $\text{L}^{2-}$ . As follows, the similar red-shift phenomenon was observed in MOF **1**.

## CONCLUSION

Herein, two new BTD-derived MOFs **1** and **2** were successfully obtained, which were structurally similar. It is interesting that one free sulfur atom was fixed in a Cd(II) cluster cage to form the SBU S@Cd<sub>6</sub>, which further extended into a 3D porous framework. MOF **1** showed a larger BET surface area (404.34 m<sup>2</sup>/g) than that of **2** (102.23 m<sup>2</sup>/g). More interestingly, uncommon BTD antidimmer was evidenced by the corresponding structural and photophysical experiment. Furthermore, because of the structural character, either **1** or **2** showed the special dual emission, the mechanism of which was realized by the structural analyses and photophysical study. Researching the solvatochromic behavior of **1** and **2** revealed that the dual emission was clearly red-shifted by increasing the solvent polarity or the acidity of ambience, respectively. These results indicate that chromophore-derived MOF can be a powerful platform to deeply understand the relationship between photophysical properties and the structures, which is extremely beneficial to design and construct the excellent optical-functional materials.

## ASSOCIATED CONTENT

### Supporting Information

The Supporting Information is available free of charge on the ACS Publications website at DOI: 10.1021/acs.inorgchem.6b02863.

Selected bond lengths and angles, PXRD, TGA, and additional figures. CCDC1504823–1504824 crystal data for **1** and **2** (CIF) (PDF)

X-ray crystallographic information (CIF)

X-ray crystallographic information (CIF)

## AUTHOR INFORMATION

### Corresponding Authors

\*E-mail: jieding@zzu.edu.cn. (J.D.)

\*E-mail: houhongw@zzu.edu.cn. (H.H.)

### ORCID

Hongwei Hou: 0000-0003-4762-0920

### Author Contributions

#Q.C. and X.H. contributed equally to the work and should be considered cofirst authors.

### Notes

The authors declare no competing financial interest.

## ACKNOWLEDGMENTS

This work was financially supported by the National Natural Science Foundation (Nos. 21371155, 21301157, and 21671174).

## REFERENCES

(1) (a) Yaghi, O. M.; Li, G. M.; Li, H. L. Selective binding and removal of guests in a microporous metal-organic framework. *Nature* **1995**, *378*, 703–706. (b) Venkataraman, D.; Gardner, G. B.; Lee, S.; Moore, J. S. Zeolite-like behavior of a coordination network. *J. Am. Chem. Soc.* **1995**, *117*, 11600–11601. (c) Kondo, M.; Yoshitomi, T.; Seki, K.; Matsuzaka, H.; Kitagawa, S. Three-dimensional framework with channeling cavities for small molecules: {[M<sub>2</sub>(4,4'-bpy)<sub>3</sub>(NO<sub>3</sub>)<sub>4</sub>•x H<sub>2</sub>O]}<sub>n</sub> (M = Co, Ni, Zn). *Angew. Chem., Int. Ed. Engl.* **1997**, *36*, 1725–1727. (d) Kitagawa, S.; Kitaura, R.; Noro, S.-I. Functional porous coordination polymers. *Angew. Chem., Int. Ed.* **2004**, *43*, 2334–2375. (e) Long, J. R.; Yaghi, O. M. The pervasive chemistry of metal-organic frameworks. *Chem. Soc. Rev.* **2009**, *38*, 1213–1214.

(2) (a) Furukawa, H.; Cordova, K. E.; O'Keeffe, M.; Yaghi, O. M. The chemistry and applications of metal-organic frameworks. *Science* **2013**, *341*, 1230444. (b) Cook, T. R.; Zheng, Y.-R.; Stang, P. J. Metal-Organic frameworks and self-assembled supramolecular coordination complexes: comparing and contrasting the design, synthesis, and functionality of metal-organic materials. *Chem. Rev.* **2013**, *113*, 734–777. (c) Sindoro, M.; Yanai, N.; Jee, A.-Y.; Granick, S. Colloidal-sized metal-organic frameworks: synthesis and applications. *Acc. Chem. Res.* **2014**, *47*, 459–469. (d) Lu, W. G.; Wei, Z. W.; Gu, Z. Y.; Liu, T. F.; Park, J.; Park, J.; Tian, J.; Zhang, M. W.; Zhang, Q.; Gentile, T., III; Bosch, M.; Zhou, H. C. Tuning the structure and function of metal-organic frameworks via linker design. *Chem. Soc. Rev.* **2014**, *43*, 5561–5593. (e) Furukawa, S.; Reboul, J.; Diring, S.; Sumida, K.; Kitagawa, S. Structuring of metal-organic frameworks at the mesoscopic/macroscopic scale. *Chem. Soc. Rev.* **2014**, *43*, 5700–5734. (f) Schneemann, A.; Bon, V.; Schwedler, I.; Senkowska, I.; Kaskel, S.; Fischer, R. A. Flexible metal-organic frameworks. *Chem. Soc. Rev.* **2014**, *43*, 6062–6096. (g) Furukawa, H.; Müller, U.; Yaghi, O. M. Heterogeneity within order” in metal-organic frameworks. *Angew. Chem., Int. Ed.* **2015**, *54*, 3417–3430. (h) Zhang, H. C.; Zou, R. Q.; Zhao, Y. L. Macrocyclic-based metal-organic frameworks. *Coord. Chem. Rev.* **2015**, *292*, 74–90. (i) Cui, Y. J.; Li, B.; He, H. J.; Zhou, W.; Chen, B. L.; Qian, G. D. Metal-organic frameworks as platforms for functional materials. *Acc. Chem. Res.* **2016**, *49*, 483–493.

(3) (a) Allendorf, M. D.; Bauer, C. A.; Bhakta, R. K.; Houk, R. J. T. Luminescent metal-organic frameworks. *Chem. Soc. Rev.* **2009**, *38*, 1330–1352. (b) Lee, J. Y.; Farha, O. K.; Roberts, J.; Scheidt, K. A.; Nguyen, S. B. T.; Hupp, J. T. Metal-organic framework materials as catalysts. *Chem. Soc. Rev.* **2009**, *38*, 1450–1459. (c) Shekhah, O.; Liu, J.; Fischer, R. A.; Wöll, C. MOF thin films: existing and future applications. *Chem. Soc. Rev.* **2011**, *40*, 1081–1106. (d) Kreno, L. E.; Leong, K.; Farha, O. K.; Allendorf, M.; van Duyne, R. P.; Hupp, J. T. Metal-organic framework materials as chemical sensors. *Chem. Rev.* **2012**, *112*, 1105–1125. (e) Horcajada, P.; Gref, R.; Baati, T.; Allan, P. K.; Maurin, G.; Couvreur, P.; Férey, G.; Morris, R. E.; Serre, C. Metal-organic frameworks in biomedicine. *Chem. Rev.* **2012**, *112*, 1232–1268. (f) Makal, T. A.; Li, J. R.; Lu, W. G.; Zhou, H. C. Methane storage in advanced porous materials. *Chem. Soc. Rev.* **2012**, *41*, 7761–7779.

(4) (a) Barea, E.; Montoro, C.; Navarro, J. A. R. Toxic gas removal-metal-organic frameworks for the capture and degradation of toxic gases and vapours. *Chem. Soc. Rev.* **2014**, *43*, 5419–5430. (b) Zhu, Q. L.; Xu, Q. Metal-organic framework composites. *Chem. Soc. Rev.* **2014**, *43*, 5468–5512. (c) Falcaro, P.; Ricco, R.; Doherty, C. M.; Liang, K.; Hill, A. J.; Styles, M. J. MOF positioning technology and device fabrication. *Chem. Soc. Rev.* **2014**, *43*, 5513–5560. (d) Liu, J. W.; Chen, L. F.; Cui, H.; Zhang, J. Y.; Zhang, L.; Su, C. Y. Applications of metal-organic frameworks in heterogeneous supramolecular catalysis. *Chem. Soc. Rev.* **2014**, *43*, 6011–6061. (e) Doherty, C. M.; Buso, D.; Hill, A. J.; Furukawa, S.; Kitagawa, S.; Falcaro, P. Using functional nano- and microparticles for the preparation of metal-organic framework composites with novel properties. *Acc. Chem. Res.* **2014**, *47*, 396–405.

(5) (a) Wales, D. J.; Grand, J.; Ting, V. P.; Burke, R. D.; Edler, K. J.; Bowen, C. R.; Mintova, S.; Burrows, A. D. Gas sensing using porous materials for automotive applications. *Chem. Soc. Rev.* **2015**, *44*, 4290–4321. (b) Silva, P.; Vilela, S. M. F.; Tome, J. P. C.; Almeida Paz, F. A. Multifunctional metal-organic frameworks: from academia to industrial applications. *Chem. Soc. Rev.* **2015**, *44*, 6774–6803. (c) Wang, L.; Han, Y. Z.; Feng, X.; Zhou, J. W.; Qi, P. F.; Wang, B. Metal-organic frameworks for energy storage: batteries and supercapacitors. *Coord. Chem. Rev.* **2016**, *307*, 361–381. (d) Aguilera-Sigalat, J.; Bradshaw, D. Synthesis and applications of metal-organic framework-quantum dot (QD@MOF) composites. *Coord. Chem. Rev.* **2016**, *307*, 267–291. (e) Li, B. Y.; Chrzanowski, M.; Zhang, Y. M.; Ma, S. Q. Applications of metal-organic frameworks featuring multi-functional sites. *Coord. Chem. Rev.* **2016**, *307*, 106–129. (f) Nath, I.; Chakraborty, J.; Verpoort, F. Metal organic frameworks mimicking natural enzymes: a

structural and functional analogy. *Chem. Soc. Rev.* **2016**, *45*, 4127–4170.

(6) (a) Evans, O. R.; Lin, W. B. Crystal engineering of NLO materials based on metal-organic coordination networks. *Acc. Chem. Res.* **2002**, *35*, 511–522. (b) Binnemans, K. Lanthanide-based luminescent hybrid materials. *Chem. Rev.* **2009**, *109*, 4283–4374. (c) Rocha, J.; Carlos, L. D.; Paz, F. A. A.; Ananias, D. Luminescent multifunctional lanthanide-based metal-organic frameworks. *Chem. Soc. Rev.* **2011**, *40*, 926–940. (d) Wang, C.; Zhang, T.; Lin, W. B. Rational Synthesis of noncentrosymmetric metal-organic frameworks for second-order nonlinear optics. *Chem. Rev.* **2012**, *112*, 1084–1104. (e) Cui, Y. J.; Yue, Y. F.; Qian, G. D.; Chen, B. L. Luminescent functional metal organic frameworks. *Chem. Rev.* **2012**, *112*, 1126–1162. (f) Zhang, W.; Xiong, R. G. Ferroelectric metal-organic frameworks. *Chem. Rev.* **2012**, *112*, 1163–1195.

(7) (a) Heine, J.; Müller-Buschbaum, K. Engineering metal-based luminescence in coordination polymers and metal-organic frameworks. *Chem. Soc. Rev.* **2013**, *42*, 9232–9242. (b) Hu, Z. C.; Deibert, B. J.; Li, J. Luminescent metal-organic frameworks for chemical sensing and explosive detection. *Chem. Soc. Rev.* **2014**, *43*, 5815–5840. (c) Cui, Y. J.; Chen, B. L.; Qian, G. D. Lanthanide metal-organic frameworks for luminescent sensing and light-emitting applications. *Coord. Chem. Rev.* **2014**, *273–274*, 76–86. (d) Stavila, V.; Talin, A. A.; Allendorf, M. D. MOF-based electronic and optoelectronic devices. *Chem. Soc. Rev.* **2014**, *43*, 5994–6010. (e) Dhakshinamoorthy, A.; Asiri, A. M.; Garcia, H. Metal-organic framework (MOF) compounds: photocatalysts for redox reactions and solar fuel production. *Angew. Chem., Int. Ed.* **2016**, *55*, 5414–5445. (f) Zhang, X. J.; Wang, W. J.; Hu, Z. J.; Wang, G. N.; Uvdal, K. Coordination polymers for energy transfer: preparations, properties, sensing applications, and perspectives. *Coord. Chem. Rev.* **2015**, *284*, 206–235. (g) Jones, C. L.; Tansell, A. J.; Easun, T. L. The lighter side of MOFs: structurally photoresponsive metal-organic frameworks. *J. Mater. Chem. A* **2016**, *4*, 6714–6723.

(8) (a) D'Andrade, B. W.; Forrest, S. R. White organic light-emitting devices for solid-state lighting. *Adv. Mater.* **2004**, *16*, 1585–1595. (b) Wang, P.; Ma, J. P.; Dong, Y. B.; Huang, R. Q. Tunable luminescent lanthanide coordination polymers based on reversible solid-state ion-exchange monitored by ion-dependent photoinduced emission spectra. *J. Am. Chem. Soc.* **2007**, *129*, 10620–10621. (c) Wang, M. S.; Guo, S. P.; Li, Y.; Cai, L. Z.; Zou, J. P.; Xu, G.; Zhou, W. W.; Zheng, F. K.; Guo, G. C. A Direct white-light-emitting metal-organic framework with tunable yellow-to-white photoluminescence by variation of excitation light. *J. Am. Chem. Soc.* **2009**, *131*, 13572–13573. (d) Sun, C. Y.; Wang, X. L.; Zhang, X.; Qin, C.; Li, P.; Su, Z. M.; Zhu, D. X.; Shan, G. G.; Shao, K. Z.; Wu, H.; Li, J. Efficient and tunable white-light emission of metal-organic frameworks by iridium-complex encapsulation. *Nat. Commun.* **2013**, *4*, 2716–2717. (e) Ma, M. L.; Qin, J. H.; Ji, C.; Xu, H.; Wang, R.; Li, B. J.; Zang, S. Q.; Hou, H. W.; Batten, S. R. Anionic porous metal-organic framework with novel 5-connected *vbk* topology for rapid adsorption of dyes and tunable white light emission. *J. Mater. Chem. C* **2014**, *2*, 1085–1093. (f) Chen, D. S.; Xing, H. Z.; Su, Z. M.; Wang, C. G. Electrical conductivity and electroluminescence of a new anthracene-based metal-organic framework with  $\pi$ -conjugated zigzag chains. *Chem. Commun.* **2016**, *52*, 2019–2022.

(9) (a) Kent, C. A.; Mehl, B. P.; Ma, L. Q.; Papanikolas, J. M.; Meyer, T. J.; Lin, W. B. Energy transfer dynamics in metal-organic frameworks. *J. Am. Chem. Soc.* **2010**, *132*, 12767–12769. (b) Zhang, X. D.; Ballem, M. A.; Hu, Z. J.; Bergman, P.; Uvdal, K. Nanoscale light-harvesting metal-organic frameworks. *Angew. Chem.* **2011**, *123*, 5847–5851. (c) Suresh, V. M.; George, S. J.; Maji, T. K. MOF nano-vesicles and toroids: self-assembled porous soft-hybrids for light harvesting. *Adv. Funct. Mater.* **2013**, *23*, 5585–5590. (d) Sun, L. B.; Xing, H. Z.; Liang, Z. Q.; Yu, J. H.; Xu, R. R. A 4 + 4 strategy for synthesis of zeolitic metal-organic frameworks: an indium-MOF with SOD topology as a light-harvesting antenna. *Chem. Commun.* **2013**, *49*, 11155–11157. (e) Foster, M. E.; Azoulay, J. D.; Wong, B. M.; Allendorf, M. D. Novel metal-organic framework linkers for light harvesting applications. *Chem. Sci.* **2014**, *5*, 2081–2090. (f) So, M. C.;

Wiederrecht, G. P.; Mondloch, J. E.; Hupp, J. T.; Farha, O. K. Metal-organic framework materials for light-harvesting and energy transfer. *Chem. Commun.* **2015**, *51*, 3501–3510. (g) Lee, D. Y.; Lim, I.; Shin, C. Y.; Patil, S. A.; Lee, W.; Shrestha, N. K.; Lee, J. K.; Han, S. H. Facile interfacial charge transfer across hole doped cobalt-based MOFs/TiO<sub>2</sub> nano-hybrids making MOFs light harvesting active layers in solar cells. *J. Mater. Chem. A* **2015**, *3*, 22669–22676. (h) Han, S. B.; Warren, S. C.; Yoon, S. M.; Malliakas, C. D.; Hou, X. L.; Wei, Y. H.; Kanatzidis, M. G.; Grzybowski, B. A. Tunneling electrical connection to the interior of metal-organic frameworks. *J. Am. Chem. Soc.* **2015**, *137*, 8169–8175. (i) Williams, D. E.; Shustova, N. B. Metal-organic frameworks as a versatile tool to study and model energy transfer processes. *Chem. - Eur. J.* **2015**, *21*, 15474–15479. (j) Zhang, Q. Q.; Zhang, C. K.; Cao, L. Y.; Wang, Z.; An, B.; Lin, Z. K.; Huang, R. Y.; Zhang, Z. M.; Wang, C.; Lin, W. B. Förster energy transport in metal-organic frameworks is beyond step-by-step hopping. *J. Am. Chem. Soc.* **2016**, *138*, 5308–5315.

(10) (a) Zang, S. Q.; Su, Y.; Li, Y. Z.; Ni, Z. P.; Meng, Q. J. Assemblies of a new flexible multicarboxylate ligand and d<sup>10</sup> metal centers toward the construction of homochiral helical coordination polymers: structures, luminescence, and NLO-active properties. *Inorg. Chem.* **2006**, *45*, 174–180. (b) Yang, J.; Li, G. D.; Cao, J. J.; Yue, Q.; Li, G.-H.; Chen, J. S. Structural variation from 1D to 3D: effects of ligands and solvents on the construction of lead(II)-organic coordination polymers. *Chem. - Eur. J.* **2007**, *13*, 3248–3261. (c) Huang, K. X.; Song, Y. L.; Pan, Z. R.; Li, Y. Z.; Zhuo, X.; Zheng, H. G. Porous nonlinear-optical material based on a twin-nest-shaped heterothiometallic cluster: {[NH<sub>4</sub>][W<sub>2</sub>O<sub>2</sub>S<sub>6</sub>Cu<sub>6</sub>I<sub>3</sub>(4,4'-bipy)<sub>4</sub>•5H<sub>2</sub>O]<sub>n</sub>}. *Inorg. Chem.* **2007**, *46*, 6233–6235. (d) Wei, Z. H.; Ni, C. Y.; Li, H. X.; Ren, Z.-G.; Sun, Z. R.; Lang, J. P. [PyH][{TpMo( $\mu$ -S)<sub>4</sub>Cu<sub>3</sub>}( $\mu$ <sub>12</sub>-1)}]: a unique tetracubane cluster derived from the S-S bond cleavage and the iodide template effects and its enhanced NLO performances. *Chem. Commun.* **2013**, *49*, 4836–4838. (e) Zhang, Z. Y.; Gong, W. G.; Wang, F.; Chen, M. M.; Zhou, L. K.; Ren, Z. G.; Sun, Z. R.; Lang, J. P. Assembly of new Mo/Cu/S clusters from [Et<sub>4</sub>N]-[Tp\*MoS(S<sub>4</sub>)] and Cu(I) salts: syntheses, structures and third-order nonlinear optical properties. *Dalton Trans.* **2013**, *42*, 9495–9504. (f) He, Y. P.; Tan, Y. X.; Zhang, J. Gas sorption, second-order nonlinear optics, and luminescence properties of a multifunctional sr-type metal-organic framework built by tris(4-carboxylphenyl)durylamine. *Inorg. Chem.* **2015**, *54*, 6653–6656. (g) Li, J. H.; Jia, D.; Meng, S.; Zhang, J. F.; Cifuentes, M. P.; Humphrey, M. G.; Zhang, C. Tetrazine chromophore-based metal-organic frameworks with unusual configurations: synthetic, structural, theoretical, fluorescent, and nonlinear optical studies. *Chem. - Eur. J.* **2015**, *21*, 7914–7926. (h) Liu, M.; Quah, H. S.; Wen, S. C.; Yu, Z. S.; Vittal, J. J.; Ji, W. Efficient third harmonic generation in a metal-organic framework. *Chem. Mater.* **2016**, *28*, 3385–3390. (i) Zhang, W. H.; Ren, Z. G.; Lang, J. P. Rational construction of functional molybdenum (tungsten)-copper-sulfur coordination oligomers and polymers from preformed cluster precursors. *Chem. Soc. Rev.* **2016**, *45*, 4995–5019.

(11) (a) Kataoka, Y.; Sato, K.; Miyazaki, Y.; Masuda, K.; Tanaka, H.; Naito, S.; Mori, W. Photocatalytic hydrogen production from water using porous material [Ru<sub>2</sub>(*p*-BDC)<sub>2</sub>]<sub>n</sub>. *Energy Environ. Sci.* **2009**, *2*, 397–400. (b) Dan-Hardi, M.; Serre, C.; Frot, T.; Rozes, L.; Maurin, G.; Sanchez, C.; Férey, G. A new photoactive crystalline highly porous titanium(IV) dicarboxylate. *J. Am. Chem. Soc.* **2009**, *131*, 10857–10859. (c) deKrafft, K. E.; Wang, C.; Lin, W. B. Metal-organic framework templated synthesis of Fe<sub>2</sub>O<sub>3</sub>/TiO<sub>2</sub> nanocomposite for hydrogen production. *Adv. Mater.* **2012**, *24*, 2014–2018. (d) He, J.; Yan, Z. Y.; Wang, J. Q.; Xie, J.; Jiang, L.; Shi, Y. M.; Yuan, F. G.; Yu, F.; Sun, Y. J. Significantly enhanced photocatalytic hydrogen evolution under visible light over CdS embedded on metal-organic frameworks. *Chem. Commun.* **2013**, *49*, 6761–6763. (e) Fateeva, A.; Chater, P. A.; Ireland, C. P.; Tahir, A. A.; Khimyak, Y. Z.; Wiper, P. V.; Darwent, J. R.; Rosseinsky, M. J. A water-stable porphyrin-based metal-organic framework active for visible-light photocatalysis. *Angew. Chem.* **2012**, *124*, 7558–7562. (f) Wang, C.; DeKrafft, K. E.; Lin, W. B. Pt nanoparticles@photoactive metal-organic frameworks: efficient hydro-

gen evolution via synergistic photoexcitation and electron injection. *J. Am. Chem. Soc.* **2012**, *134*, 7211–7214. (g) Zhou, T. H.; Du, Y. H.; Borgna, A.; Hong, J. D.; Wang, Y. B.; Han, J. Y.; Zhang, W.; Xu, R. Post-synthesis modification of a metal-organic framework to construct a bifunctional photocatalyst for hydrogen production. *Energy Environ. Sci.* **2013**, *6*, 3229–3234.

(12) (a) Meng, W.; Xu, Z. Q.; Ding, J.; Wu, D. Q.; Han, X.; Hou, H. W.; Fan, Y. T. A systematic research on the synthesis, structures, and application in photocatalysis of cluster-based coordination complexes. *Cryst. Growth Des.* **2014**, *14*, 730–738. (b) Li, R.; Ren, X. Q.; Ma, H. W.; Feng, X.; Lin, Z. G.; Li, X. G.; Hu, C. W.; Wang, B. Nickel-substituted zeolitic imidazolate frameworks for time-resolved alcohol sensing and photocatalysis under visible light. *J. Mater. Chem. A* **2014**, *2*, 5724–5729. (c) Kong, X. J.; Lin, Z. K.; Zhang, Z. M.; Zhang, T.; Lin, W. B. Hierarchical integration of photosensitizing metal-organic frameworks and nickel-containing polyoxometalates for efficient visible-light-driven hydrogen evolution. *Angew. Chem., Int. Ed.* **2016**, *55*, 6411–6416. (d) Chen, D. S.; Xing, H. Z.; Wang, C. G.; Su, Z. M. Highly efficient visible-light-driven CO<sub>2</sub> reduction to formate by a new anthracene-based zirconium MOF via dual catalytic routes. *J. Mater. Chem. A* **2016**, *4*, 2657–2662.

(13) (a) Zhao, B.; Chen, X. Y.; Cheng, P.; Liao, D. Z.; Yan, S.-P.; Jiang, Z. H. Coordination polymers containing 1D channels as selective luminescent probes. *J. Am. Chem. Soc.* **2004**, *126*, 15394–15395. (b) Lee, E. Y.; Jang, S. Y.; Suh, M. P. Multifunctionality and crystal dynamics of a highly stable, porous metal-organic framework [Zn<sub>4</sub>O(NTB)<sub>2</sub>]. *J. Am. Chem. Soc.* **2005**, *127*, 6374–6381. (c) Zhu, W.-H.; Wang, Z.-M.; Gao, S. Two 3D porous lanthanide-fumarate-oxalate frameworks exhibiting framework dynamics and luminescent change upon reversible deand rehydration. *Inorg. Chem.* **2007**, *46*, 1337–1342. (d) Lu, W. G.; Jiang, L.; Feng, X. L.; Lu, T. B. Three-dimensional lanthanide anionic metal-organic frameworks with tunable luminescent properties induced by cation exchange. *Inorg. Chem.* **2009**, *48*, 6997–6999. (e) Harbuzaru, B. V.; Corma, A.; Rey, F.; Jordá, J. L.; Ananias, D.; Carlos, L. D.; Rocha, J. A miniaturized linear pH sensor based on a highly photoluminescent self-assembled europium(III) metal-organic framework. *Angew. Chem., Int. Ed.* **2009**, *48*, 6476–6479. (f) Xie, Z. G.; Ma, L. Q.; deKrafft, K. E.; Jin, A.; Lin, W. B. Porous phosphorescent coordination polymers for oxygen sensing. *J. Am. Chem. Soc.* **2010**, *132*, 922–923. (g) Guo, Z.; Xu, H.; Su, S.; Cai, J.; Dang, S.; Xiang, S.; Qian, G.; Zhang, H.; O’Keefe, M.; Chen, B. A robust near infrared luminescent ytterbium metal-organic framework for sensing of small molecules. *Chem. Commun.* **2011**, *47*, 5551–5553. (h) Ferrando-Soria, J.; Khajavi, H.; Serra-Crespo, P.; Gascon, J.; Kapteijn, F.; Julve, M.; Lloret, F.; Pasán, J.; Ruiz-Pérez, C.; Journaux, Y.; Pardo, E. Highly selective chemical sensing in a luminescent nanoporous magnet. *Adv. Mater.* **2012**, *24*, 5625–5629.

(14) (a) Wang, J. H.; Li, M.; Li, D. A dynamic, luminescent and entangled MOF as a qualitative sensor for volatile organic solvents and a quantitative monitor for acetonitrile vapour. *Chem. Sci.* **2013**, *4*, 1793–1801. (b) Song, X. Z.; Song, S. Y.; Zhao, S. N.; Hao, Z. M.; Zhu, M.; Meng, X.; Wu, L. L.; Zhang, H. J. Single-crystal-to-single-crystal transformation of a europium(III) metal-organic framework producing a multi-responsive luminescent sensor. *Adv. Funct. Mater.* **2014**, *24*, 4034–4041. (c) Nickerl, G.; Senkowska, I.; Kaskel, S. Tetrazine functionalized zirconium MOF as an optical sensor for oxidizing gases. *Chem. Commun.* **2015**, *51*, 2280–2282. (d) Cui, Y. J.; Zhu, F. L.; Chen, B. L.; Qian, G. D. Metal-organic frameworks for luminescence thermometry. *Chem. Commun.* **2015**, *51*, 7420–7431. (e) Ye, J. W.; Zhou, H. L.; Liu, S. Y.; Cheng, X. N.; Lin, R. B.; Qi, X. L.; Zhang, J. P.; Chen, X. M. Encapsulating pyrene in a metal-organic zeolite for optical sensing of molecular oxygen. *Chem. Mater.* **2015**, *27*, 8255–8260. (f) Zhao, J.; Wang, Y. N.; Dong, W. W.; Wu, Y. P.; Li, D. S.; Zhang, Q. C. A robust luminescent Tb(III)-MOF with lewis basic pyridyl sites for the highly sensitive detection of metal ions and small molecules. *Inorg. Chem.* **2016**, *55*, 3265–3271.

(15) Li, M.; Yao, Y.; Ding, J.; Liu, L.; Qin, J. H.; Zhao, Y. P.; Hou, H. W.; Fan, Y. T. Spectroscopic and crystallographic investigations of

novel BODIPY-derived metal-organic frameworks. *Inorg. Chem.* **2015**, *54*, 1346–1353.

(16) (a) Chen, J. W.; Cao, Y. Development of novel conjugated donor polymers for high-efficiency bulk-heterojunction photovoltaic devices. *Acc. Chem. Res.* **2009**, *42*, 1709–1718. (b) Beaujuge, P. M.; Amb, C. M.; Reynolds, J. R. Spectral engineering in  $\pi$ -conjugated polymers with intramolecular donor-acceptor interactions. *Acc. Chem. Res.* **2010**, *43*, 1396–1407. (c) Li, Y. F. Molecular design of photovoltaic materials for polymer solar cells: toward suitable electronic energy levels and broad absorption. *Acc. Chem. Res.* **2012**, *45*, 723–733. (d) Neto, B. A. D.; Lapis, A. A. M.; da Silva Júnior, E. N.; Dupont, J. 2,1,3-Benzothiadiazole and derivatives: synthesis, properties, reactions, and applications in light technology of small molecules. *Eur. J. Org. Chem.* **2013**, *2013*, 228–255. (e) Parker, T. C.; Pa-tel, D. G.; Moudgil, K.; Barlow, S.; Risko, C.; Brédas, J. L.; Reynolds, J. R.; Marder, S. R. Heteroannulated acceptors based on benzothiadiazole. *Mater. Horiz.* **2015**, *2*, 22–36. (f) Neto, B. A. D.; Carvalho, P. H. P. R.; Correa, J. R. *Acc. Chem. Res.* **2015**, *48*, 1560–1569.

(17) (a) Espinet, P.; Echavarren, A. M. The mechanisms of the stille reaction. *Angew. Chem., Int. Ed.* **2004**, *43*, 4704–4734. (b) Suzuki, A. Carbon-carbon bonding made easy. *Chem. Commun.* **2005**, *38*, 4759–4763. (c) Sonar, P.; Singh, S. P.; Sudhakar, S.; Dodabalapur, A.; Sellinger, A. High-mobility organic thin film transistors based on benzothiadiazole-sandwiched dihexylquaterthiophenes. *Chem. Mater.* **2008**, *20*, 3184–3190. (d) Zhu, W. H.; Meng, X. L.; Yang, Y. H.; Zhang, Q.; Xie, Y. S.; Tian, H. Bisthiénylenehexanes containing a benzothiadiazole unit as a bridge: photochromic performance dependence on substitution position. *Chem. - Eur. J.* **2010**, *16*, 899–906. (e) Shen, M.; Rodríguez-López, J.; Huang, J.; Liu, Q.; Zhu, X. H.; Bard, A. J. Electrochemistry and electrogenerated chemiluminescence of dithienylbenzothiadiazole derivative. differential reactivity of donor and acceptor groups and simulations of radical cation-anion and dication-radical anion annihilations. *J. Am. Chem. Soc.* **2010**, *132*, 13453–13461.

(18) (a) Lin, R. Y. Y.; Lee, C. P.; Chen, Y. C.; Peng, J. D.; Chu, T. C.; Chou, H. H.; Yang, H. M.; Lin, J. T.; Ho, K. C. Benzothiadiazole-containing donor-acceptor-acceptor type organic sensitizers for solar cells with ZnO photoanodes. *Chem. Commun.* **2012**, *48*, 12071–12073. (b) Sonar, P.; Williams, E. L.; Singh, S. P.; Manzhos, S.; Dodabalapur, A. A benzothiadiazole end capped donor-acceptor based small molecule for organic electronics. *Phys. Chem. Chem. Phys.* **2013**, *15*, 17064–17069. (c) Pop, F.; Amacher, A.; Avarvari, N.; Ding, J.; Daku, L. M. L.; Hauser, A.; Koch, M.; Hauser, J.; Liu, S. X.; Decurtins, S. Tetrathiafulvalene-benzothiadiazoles as redox-tunable donor-acceptor systems: synthesis and photophysical study. *Chem. - Eur. J.* **2013**, *19*, 2504–2514.

(19) (a) Yang, G.; Di, C. A.; Zhang, G. X.; Zhang, J.; Xiang, J. F.; Zhang, D. Q.; Zhu, D. Highly sensitive chemical-vapor sensor based on thin-film organic field-effect transistors with benzothiadiazole-fused-tetrathiafulvalene. *Adv. Funct. Mater.* **2013**, *23*, 1671–1676. (b) Tucker, N. M.; Briseno, A. L.; Acton, O.; Yip, H. L.; Ma, H.; Jenekhe, S. A.; Xia, Y. N.; Jen, A. K. Y. Solvent-dispersed benzothiadiazole-tetrathiafulvalene single-crystal nanowires and their application in field-effect transistors. *ACS Appl. Mater. Interfaces* **2013**, *5*, 2320–2324. (c) Gautam, P.; Misra, R.; Siddiqui, S. A.; Sharma, G. D. Unsymmetrical donor-acceptor-acceptor- $\pi$ -donor type benzothiadiazole-based small molecule for a solution processed bulk heterojunction organic solar cell. *ACS Appl. Mater. Interfaces* **2015**, *7*, 10283–10292.

(20) (a) van Vooren, A.; Kim, J.-S., Prof.; Cornil, J., Dr. Intrachain versus interchain electron transport in poly(fluorene-*alt*-benzothiadiazole): a quantum-chemical insight. *ChemPhysChem* **2008**, *9*, 989–993. (b) Watanabe, M.; Goto, K.; Fujitsuka, M.; Tojo, S.; Majima, T.; Shinmyozu, T. 2,1,3-Benzothiadiazole dimers: preparation, structure, and transannular electronic interactions of *syn*- and *anti*-[2.2](4,7)-benzothiadiazolophanes. *Bull. Chem. Soc. Jpn.* **2010**, *83*, 1155–1161.

(21) Song, C. L.; He, Y. B.; Li, B.; Ling, Y. J.; Wang, H. L.; Feng, Y. L.; Krishna, R.; Chen, B. L. Enhanced CO<sub>2</sub> sorption and selectivity by functionalization of a NbO-type metal-organic framework with

polarized benzothiadiazole moieties. *Chem. Commun.* **2014**, *50*, 12105–12108.

(22) Agneeswari, R.; Tamilavan, V.; Song, M.; Hyun, M. H. Property modulation of benzodithiophene-based polymers via the incorporation of a covalently bonded novel 2,1,3-benzothiadiazole-1,2,4-oxadiazole derivative in their main chain for polymer solar cells. *J. Mater. Chem. C* **2014**, *2*, 8515–8524.

(23) Sheldrick, G. M. A short history of SHELX. *Acta Crystallogr., Sect. A: Found. Crystallogr.* **2008**, *A64*, 112–122.

(24) Orpen, A. G.; Brammer, L.; Allen, F. H.; Kennard, O.; Watson, D. G.; Taylor, R. Tables of bond lengths determined by X-Ray and neutron diffraction. Part 2. Organometallic compounds and Coordination complexes of the *d*- and *f*-block metals. *J. Chem. Soc., Dalton Trans.* **1989**, S1–S83.

(25) DaSilveira Neto, B. A.; Lopes, A. S. A.; Ebeling, G.; Gonçalves, R. S.; Costa, V. E. U.; Quina, F. H.; Dupont, J. Photophysical and electrochemical properties of  $\pi$ -extended molecular 2,1,3-benzothiadiazoles. *Tetrahedron* **2005**, *61*, 10975–10982.